cMat

WILEY

有科出版 YOUKE PUBLISHING

ORIGINAL ARTICLE OPEN ACCESS

Effects of the Melt Temperature on Cluster Structures and Mechanical Properties of FeCoNi-Based High-Entropy Bulk Metallic Glasses

Xue-Ru Fan[1] | Lei Xie[2] | Qiang Li[3,4] | Yun-He Gao[5] | Chun-Tao Chang[2] | Meng Gao[5]

[1]School of Physics Science and Technology, Xinjiang University, Urumqi, China | [2]School of Mechanical Engineering, Neutron Scattering Technical Engineering Research Center, Dongguan University of Technology, Dongguan, China | [3]School of Materials Science and Engineering, Xinjiang University, Urumqi, China | [4]Xinjiang Environmental Functional Materials Engineering Technology Research Center, Xinjiang University, Urumqi, China | [5]CAS Key Laboratory of Magnetic Materials and Devices, and Zhejiang Province Key Laboratory of Magnetic Materials and Application Technology, Ningbo Institute of Materials Technology and Engineering, Chinese Academy of Sciences, Ningbo, China

Correspondence: Qiang Li (qli@xju.edu.cn) | Chun-Tao Chang (changct@dgut.edu.cn) | Meng Gao (gaomeng@nimte.ac.cn)

Received: 28 April 2025 | **Revised:** 12 May 2025 | **Accepted:** 23 May 2025

Keywords: cluster structure | high-entropy bulk metallic glass | melt temperature | nanoscale heterogeneity | plasticity

ABSTRACT

This study investigates the influence of melt temperature on the structure and mechanical properties of $[Fe_{0.25}Co_{0.25}Ni_{0.25}(Si_{0.3}B_{0.7})_{0.25}]_{99.7}Cu_{0.3}$ high-entropy bulk metallic glasses (HE-BMGs). Samples were prepared at varying melt temperatures (1423, 1523, 1573, and 1623 K) using the J-quenching technique. The results reveal that melt temperature significantly affects the atomic arrangement structures, which in turn impacts plasticity and thermal stability. At a lower melt temperature (1423 K), crystal-like clusters form, leading to poor plasticity due to stress concentrations. In contrast, melt temperatures within an optimal range (1523–1573 K) promote a more uniform distribution of soft and hard zones, enhancing plastic deformation. Specifically, the sample prepared in 1573 K melt temperature exhibited the best plasticity, attributed to favorable structural nonuniformity and an increased proportion of soft zones. However, at a higher melt temperature (1623 K), excessive superheating resulted in the formation of large Cu clusters, which enhanced strength but compromised plasticity due to stress concentrations. This work provides a comprehensive understanding of how melt temperature controls microstructural evolution and its influence on the mechanical properties of HE-BMGs, offering valuable insights for optimizing their preparation.

1 | Introduction

High-entropy bulk metallic glass (HE-BMG) combines the advantageous characteristics of the composition diversity of high-entropy alloy and the structural disorder of metallic glass (MG), resulting in exceptional properties such as high strength, hardness, corrosion resistance, and wear resistance [1, 2]. However, the absence of grain boundaries and dislocations due to atomic disorder leads to the rapid formation of shear bands during deformation, limiting its room-temperature plasticity [3]. This constraint significantly hampers its broader application in structural engineering.

The mechanical deformation behavior of alloy materials can be effectively improved by modifying their intrinsic microstructure distribution. For example, Zhao et al. enhanced the plasticity of $Fe_{34}Co_{34}Nb_6B_{27}$ BMG by 2.3% through Cu-induced phase separation [4]. Di et al. subjected $[(Fe_{0.5}Co_{0.5})_{0.75}B_{0.2}Si_{0.05}]_{96}Nb_4$ BMG to low-temperature thermal cycling treatments at different upper limit temperatures, demonstrating that controlled precipitation of ordered phase structures improves plastic properties [5]. The addition of Al to AlCoCrFeNiCu high-entropy alloy transformed the structure from a single face-centered cubic (FCC) solid solution phase to a mixed FCC and body-centered cubic phase structure, thereby enhancing the plasticity [6].

Jiang et al. introduced that uniformly dispersed particle precipitates into the $AlCrFeNi_2Ti_{0.5}$ bulk high-entropy alloy through heat treatment, maintaining the inter-dendritic structure as a single solid solution phase while improving both strength and ductility [7]. However, for HE-BMGs, despite their superior comprehensive performance, there is limited research on improving plasticity, particularly through microstructural evolution. Li et al. enhanced plasticity of $(Fe_{1/3}Co_{1/3}Ni_{1/3})_{80}(P_{1/1}B_{1/1})_{20}$ HE-BMGs by micro-adding Cr, which promoted local solute-centered atomic clusters, increased free volume content, and improved plasticity [8]. This underscores the critical role of microstructural evolution in determining the plasticity of HE-BMGs.

HE-BMGs exhibit a long-range disordered and short-range ordered amorphous structure, formed by the rapid "freezing" of metal atoms in the molten state. The melt temperature significantly influences the resulting melt structure, which in turn affects the amorphous formation and mechanical properties of the alloys [9, 10]. For example, Cui et al. prepared $Zr_{57}Cu_{20}Al_{10}Ni_8Ag_5$ BMG via copper mold spray casting at varying melt temperatures [11]. They observed a continuous decline in plasticity with increasing melt temperature, attributing this to the reduction of nanocrystalline clusters in the melt due to the increase of melt temperature. In contrast, Zhu et al. [12] studied $La_{62}Al_{14}(Cu_{5/6}Ag_{1/6})_{14}(Ni_{1/2}Co_{1/2})_{10}$ BMGs and found that plasticity at room temperature improved with higher melt temperatures. These results suggest that melt temperature impacts different alloy systems differently. Despite these findings, there remains a lack of studies focusing on the effects of melt temperature, especially for HE-BMGs, where the unique hysteresis diffusion effect is closely linked to temperature. Therefore, further investigation into the influence of melt temperature on the structure and properties of HE-BMGs is essential to elucidate the underlying mechanisms. Additionally, controlling the melt temperature accurately, which is essential for producing materials with desired properties, is an urgent technical challenge in industrial manufacturing. This study is of significance for large-scale production, where infrared thermometers, as employed by Cui et al. [11], can enable real-time temperature monitoring. Once the target melt temperature is identified, the material is maintained at this temperature for a specific duration to fabricate samples accordingly.

This study investigates the $[Fe_{0.25}Co_{0.25}Ni_{0.25}(Si_{0.3}B_{0.7})_{0.25}]_{99.7}Cu_{0.3}$ HE-BMG, which demonstrated improved plasticity through the action of phase-separated structures [13]. The HE-BMG samples were fabricated at different melt temperatures using the J-quenching technique. The effects of varying melt temperatures on deformation behavior, cluster structure, and nano-structural heterogeneity of the present HE-BMG were systematically investigated. Results demonstrate that the melting temperature significantly influences the atomic arrangement of the HE-BMG, thereby affecting their plasticity. This work not only clarifies the underlying mechanism by which melt temperature impacts microstructure and plasticity, but also provides theoretical insights and practical guidance for optimizing the preparation process of HE-BMGs.

2 | Experimental

The $[Fe_{0.25}Co_{0.25}Ni_{0.25}(Si_{0.3}B_{0.7})_{0.25}]_{99.7}Cu_{0.3}$ alloy ingots were synthesized by torch-melting a mixture of high-purity Fe powders (99.98 wt%), Ni powders (99.7 wt%), Co powders (99.9 wt%), Si pieces (99.99 wt%), B powders (99.5 wt%), and Cu pieces (99.99 wt%) under an argon atmosphere. The ingots were then fluxed in a B_2O_3-CaO (3:1 mass ratio) fluxing agent at 1473 K for 4 h under a vacuum pressure of ~50 Pa. Following fluxing treatment, the alloy ingots were prepared into 1.0 mm diameter cylindrical rods by J-quenching technique at different melt temperatures, as shown in Figure 1A. The melt temperatures were set to 1423, 1523, 1573, and 1623 K, respectively, all above the liquidus point (1413 K) of the $[Fe_{0.25}Co_{0.25}Ni_{0.25}(Si_{0.3}B_{0.7})_{0.25}]_{99.7}Cu_{0.3}$ alloy, as depicted in Figure 1B. Compression testing was conducted to assess the mechanical properties of the samples, which were prepared as cylinders with an aspect ratio of 2:1. To ensure consistency during testing, all samples had parallel upper and lower surfaces.

The amorphous structure of all samples was confirmed using X-ray diffraction (XRD, Bruker D8, Germany, Cu-Kα radiation). Thermal behavior was assessed using a differential scanning calorimeter (DSC, NETZSCH DSC 404F, Germany) at a heating rate of 0.33 K s^{-1}. Quasi-static uniaxial compression tests were performed on an Instron mechanical testing machine (WANCE ETM 105D, China) at a strain rate of 5×10^{-4} s^{-1}, with five samples tested per condition to ensure reproducibility. Post-deformation morphologies were analyzed using high-resolution scanning electron microscopy (HRSEM, Hitachi SU6600, Japan). Microstructural evolution was examined via high-resolution transmission electron microscopy (HRTEM, FEI F200X, America), with image analysis performed using fast Fourier transformation (FFT) and inverse fast Fourier transformation (IFFT). Nano-indentation tests were conducted with a nano-indentation system (KLA Nano Indenter G200, America), utilizing a spherical indenter with a tip radius of 5 μm under a continuous stiffness model. Each sample was tested at 64 points with a strain rate of 0.05 s^{-1}, a maximum penetration depth of 250 nm, and a dwell time of 10 s. Nanoscale distribution of soft and hard zones was assessed with atomic force microscopy (AFM, Bruker Dimension ICON, Germany) in PeakForce Quantitative Nanomechanics (QNM) mode, scanning a 200 × 200 nm^2 area at 512 × 512 pixels resolution. Adhesive force values were derived from the withdrawing part of the force curves, as detailed in Ref. [14]. All AFM measurements were conducted in an ultra-clean room condition with a temperature of 23 ± 1°C and a relative humidity of 20%. The relaxation behavior of the samples with different melt temperatures were checked using a dynamical mechanical analysis (DMA, TA Q800) with a frequency of 1 Hz and a heating rate of 5 K min^{-1}.

3 | Results and Discussion

Figure 1C shows the DSC curves of the samples, with the inset displaying the melting and liquidus points at 1253 and 1413 K, respectively. The DSC curves of all samples demonstrate a distinct

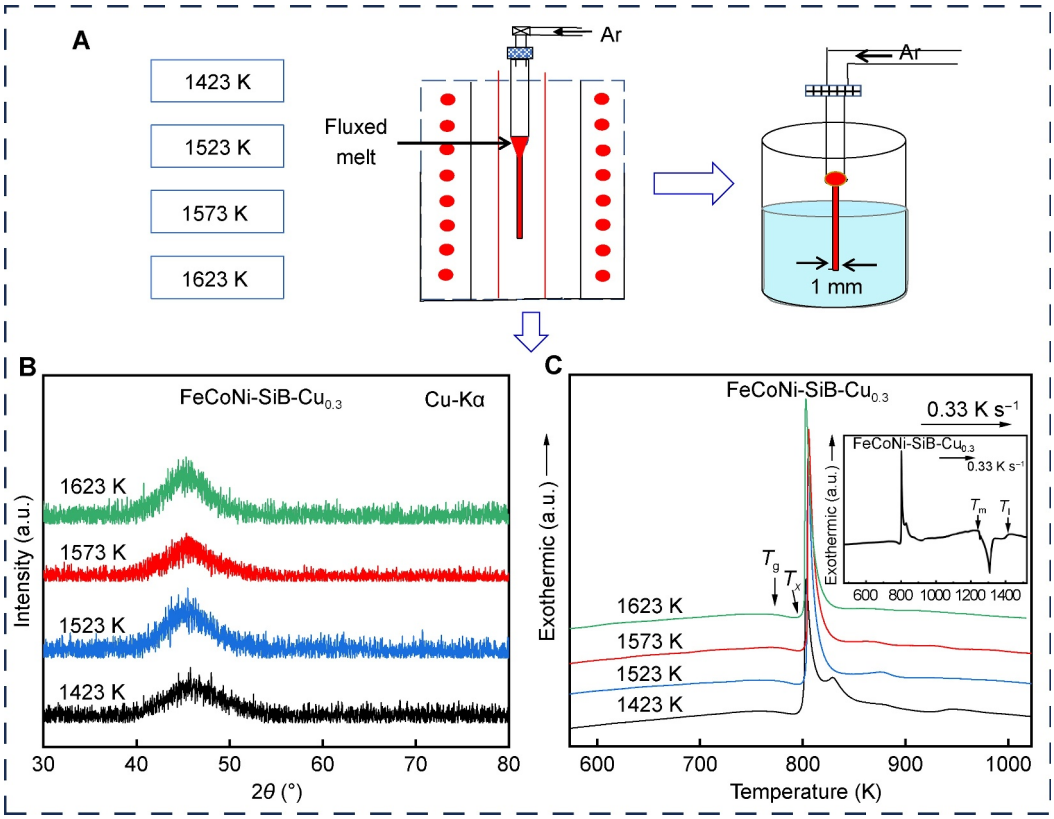

FIGURE 1 | Preparation of $[Fe_{0.25}Co_{0.25}Ni_{0.25}(Si_{0.3}B_{0.7})_{0.25}]_{99.7}Cu_{0.3}$ HE-BMGs at different melt temperatures: (A) Process diagram, (B) XRD pattern, and (C) DSC curves.

glass transition, followed by an extended supercooled liquid region and a multi-stage crystallization process, further confirming the amorphous nature. As the melt temperature increases, the glass transition temperature (T_g) and onset crystallization temperature (T_x) of $[Fe_{0.25}Co_{0.25}Ni_{0.25}(Si_{0.3}B_{0.7})_{0.25}]_{99.7}Cu_{0.3}$ HE-BMG increase, peaking before decreasing at 1623 K. This suggests the existence of an optimal melt temperature range for preparing MGs, which can enhance their thermal stability. Figure 1B presents the XRD patterns of $[Fe_{0.25}Co_{0.25}Ni_{0.25}(Si_{0.3}B_{0.7})_{0.25}]_{99.7}Cu_{0.3}$ HE-BMGs prepared at various melt temperatures (1423, 1523, 1573, and 1623 K), and the corresponding samples are hereafter referred to by their respective melting temperatures, that is, S1423, S1523, S1573, S1623. All samples exhibit a broad and smooth diffuse peak near 45° (2θ), indicating a completely amorphous structure. It is worth noting that when the melt temperature is below 1423 K, the lack of sufficient superheat prevents the successful preparation of fully amorphous bulk alloys.

The compressive stress–strain curves of $[Fe_{0.25}Co_{0.25}Ni_{0.25}(Si_{0.3}B_{0.7})_{0.25}]_{99.7}Cu_{0.3}$ HE-BMGs prepared at different melt temperatures are shown in Figure 2A. It can be observed that all samples exhibit approximately 2% elastic deformation, which is consistent with the elastic limit of most BMGs. As the melt temperature increases, the plastic strain (ε_p) shows a trend of first increasing and then decreasing. Specific analysis shows that samples with melt temperatures at low and high temperatures exhibit poor plastic deformation ability. For example, the ε_p of the S1423 and S1623 are 3.2% and 2.8%, respectively. However, when the melt temperature is in the middle range, the plastic deformation ability of the sample is significantly enhanced. The ε_p of the S1523 is approximately 4.7%, and the S1573 exhibits a value of about as high as 6.8% of ε_p. These samples also showed various degrees of variability in their ability to resist yielding. The S1423 exhibited a σ_y of 3272 MPa approximately, whereas the S1623 had a σ_y value as high as 3769 MPa. Moreover, the S1573 sample had a slightly lower σ_y than the S1523 versus the S1623, despite that it has the most excellent plastic deformation properties. The values of mechanical specific data are statistically shown in Figure 2B.

The study of fracture morphology and shear zone evolution provides valuable insights into the plastic deformation behavior of materials [15]. In this work, SEM was used to examine the morphology of $[Fe_{0.25}Co_{0.25}Ni_{0.25}(Si_{0.3}B_{0.7})_{0.25}]_{99}Cu_{0.3}$ HE-BMGs prepared at different melt temperatures after compression, as shown in Figure 3. The S1423 sample exhibits a significantly different shear fracture angle compared to the other samples with a near-vertical fracture. The corresponding microfracture morphology (Figure 3A1) shows a cleavage step pattern, indicating a lack of adhesion at the fracture. These characteristics are indicative of brittle fracture, potentially caused by shear band localization or stress concentration, making the material highly prone to rapid fracture [16]. In contrast, the lateral shear band angles of the S1523, S1573, and S1623 samples (Figure 3B–D) are all close to 45°, consistent with typically fracture angles observed in BMGs [17]. The S1573 shows clear traces of multiple shear band openings, marked with white dashed lines in Figure 3C. These shear bands, including secondary and multi-stage shear bands, are intertwined with each other, effectively

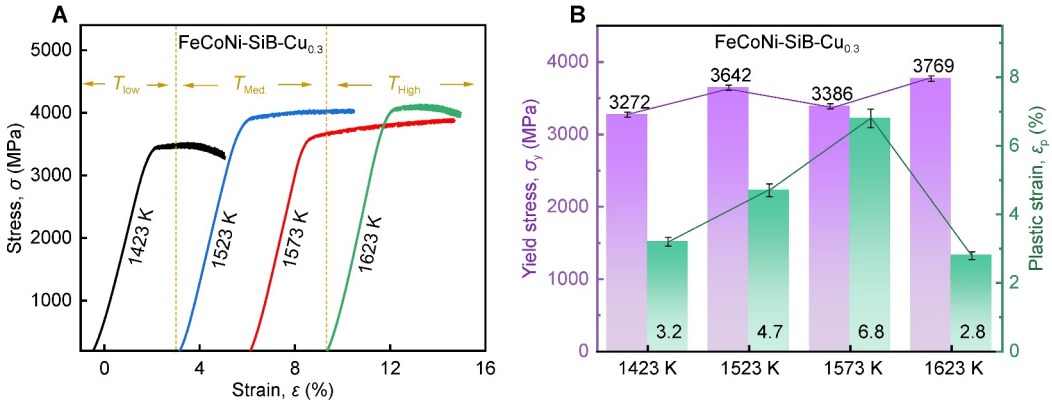

FIGURE 2 | $Fe_{0.25}Co_{0.25}Ni_{0.25}(Si_{0.3}B_{0.7})_{0.25}]_{99.7}Cu_{0.3}$ HE-BMGs (1423, 1523, 1573, and 1623 K) with (A) stress–strain curves, (B) statistical graphs of the values of ε_p and σ_y.

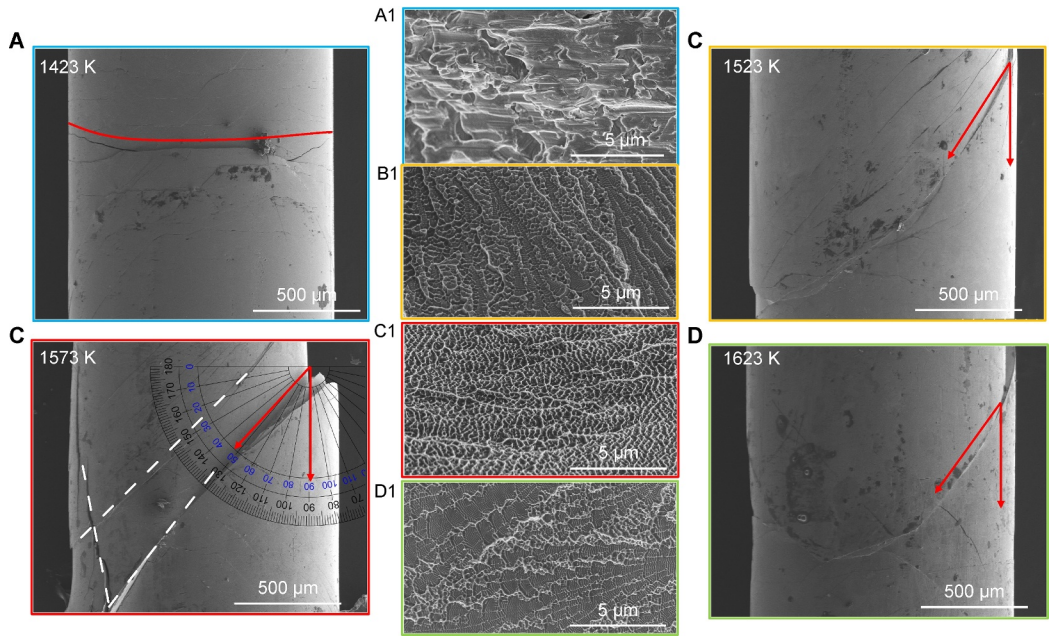

FIGURE 3 | (A–D) Side profiles of samples with different melt temperatures after deformation; (A1–D1) micro-scale SEM images of the corresponding fracture surfaces of different samples.

preventing catastrophic fracture along a single shear band. The microscopic fracture morphology of the S1573 (Figure 3C1) exhibits a standard honeycomb pattern, suggesting a certain degree of tearing and adhesion phenomenon, which is indicative of plastic deformation during fracture. The S1523 (Figure 3B) and S1623 (Figure 3D) samples show fewer shear bands than the S1573 sample. Their fracture morphology consists of tough fossa patterns and randomly distributed fishbone patterns, typical of brittle fracture [18], indicating lower plastic deformation capacity compared to the S1573 sample.

To investigate the deformation mechanism and its correlation with the mechanical properties through microstructural evolution, Figure 4A–D shows the TEM morphologies of the S1423, S1523, S1573, and S1623 samples, with the corresponding selected area electron diffraction (SAED) patterns inset in the upper left corner. The TEM images of the S1623 sample reveal fine, uniformly distributed particles, whereas no structure is observed in the other samples. The SAED patterns of all samples exhibit typical amorphous halos. To identify the composition of the nonuniform structures in the samples, high-resolution HAADF imaging was performed, as shown in Figure 4E–H. Comparison of electron scattering contrast clearly shows different particle distributions across the samples. The S1423 sample (Figure 4E) contains small-scale cluster structures, whereas the S1523 sample (Figure 4F) has granular structures about 1–2 nm in size. The S1573 sample (Figure 4G) also shows 1–2 nm granular structures, though they are less distinct. The S1623 sample (Figure 4H) exhibits a uniformly distributed cluster structure larger than 5 nm, and the inset in the upper right corner of Figure 4H illustrates the distribution of these clusters over a larger region. Elemental distribution analysis of the HAADF images (Figure 4E–H) reveals that the clusters in the S1623 sample are Cu clusters, whereas the nonuniform structures in the other samples could not be identified due to limitations in structural scale and instrument resolution. Region line scans were performed on all samples, but due to

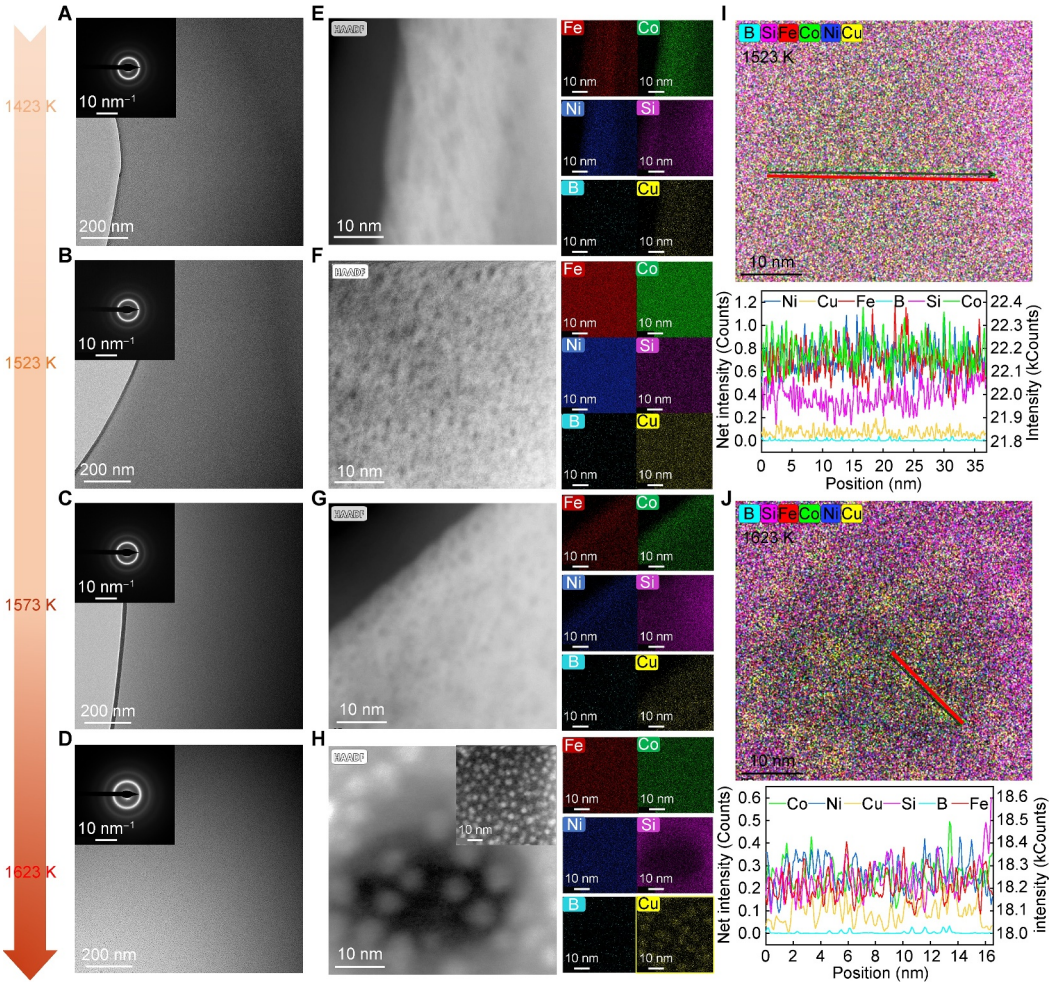

FIGURE 4 | (A–D) TEM images of samples prepared at different melt temperatures; (E–H) HAADF images along with corresponding elemental distributions; regional line-scan analyses of (I) S1523 and (J) S1623 samples.

the low resolution of the nonuniform structures in Figure 4E,G, only the region line scan of the S1523 sample (Figure 4I) is presented. This scan shows compositional fluctuations in Fe, Co, and Ni, but no significant variations in other elements. In contrast, the Cu distribution in the S1623 sample (Figure 4J) shows pronounced undulations, confirming the presence of Cu clusters at high melt temperatures.

To investigate the in-depth evolution of the short- and medium-order structures in $[Fe_{0.25}Co_{0.25}Ni_{0.25}(Si_{0.3}B_{0.7})_{0.25}]_{99}Cu_{0.3}$ HE-BMGs with the melt temperature, two-dimensional (2D) autocorrelation analyses were conducted on HRTEM images of the samples. The HRTEM images of the S1423, S1523, and S1573 samples at a scale of 10 nm were shown in Figure 5A–C. A 10×10 nm^2 square was randomly selected from each image for inverse Fourier transform (IFFT), and then divided into 100 parts of 1 nm $\times$ 1 nm square regions for 2D autocorrelation analysis (ACF), as shown in Figure 5A1–5C1. The size of each small square corresponds well with the reported size of short-range ordered (SRO) structure [19], with ordered structures marked by red squares in their HRTEM images. Quantitative analysis reveals that the proportion of SRO structure decreases with increasing the melt temperature, from 25% in the 1423 K sample to 18% in the S1523 sample, and 13% in the S1573 sample, indicating increased disorder with higher melt temperatures.

The HRTEM image of the S1423 sample (Figure 5A) shows a small amount of ordered structures, enlarged in the inset. The lattice spacing of the cluster structure is approximately 2.111 Å, close to the (111) crystal face of α-Fe phase. In addition, a Co_2B-like phase with a lattice spacing of 1.988 Å (not labeled in the figure) and an average size of about 2–3 nm is presented in these structures. This medium-range ordered (MRO) structure, prone to stress-induced brittleness at the boundary with the amorphous matrix [16], contributes to the poor plasticity of the S1423 sample. This phenomenon is primarily attributed to the hereditary effect of the melt. The positive mixing enthalpies between the elements Cu and Fe, Co and Ni, which are shown in Figure 5G, promote the formation of Cu-rich or Fe/Co/Ni rich clusters in the alloy melt. When the melt temperature is low, insufficient superheat prevents these clusters from fully dispersing, resulting in their retention in the MG.

As the melt temperature increases, the S1523 sample exhibits more distributed and dispersed ordered structures, as shown in Figure 5B1, which can act as pinning sites during deformation, hindering crack or shear band propagation and improving plasticity. However, mechanical tests revealed that the S1573 sample exhibits the best plasticity, suggesting that other microstructural factors, in addition to the structural evolution discussed, influence the mechanical properties, which will be addressed later.

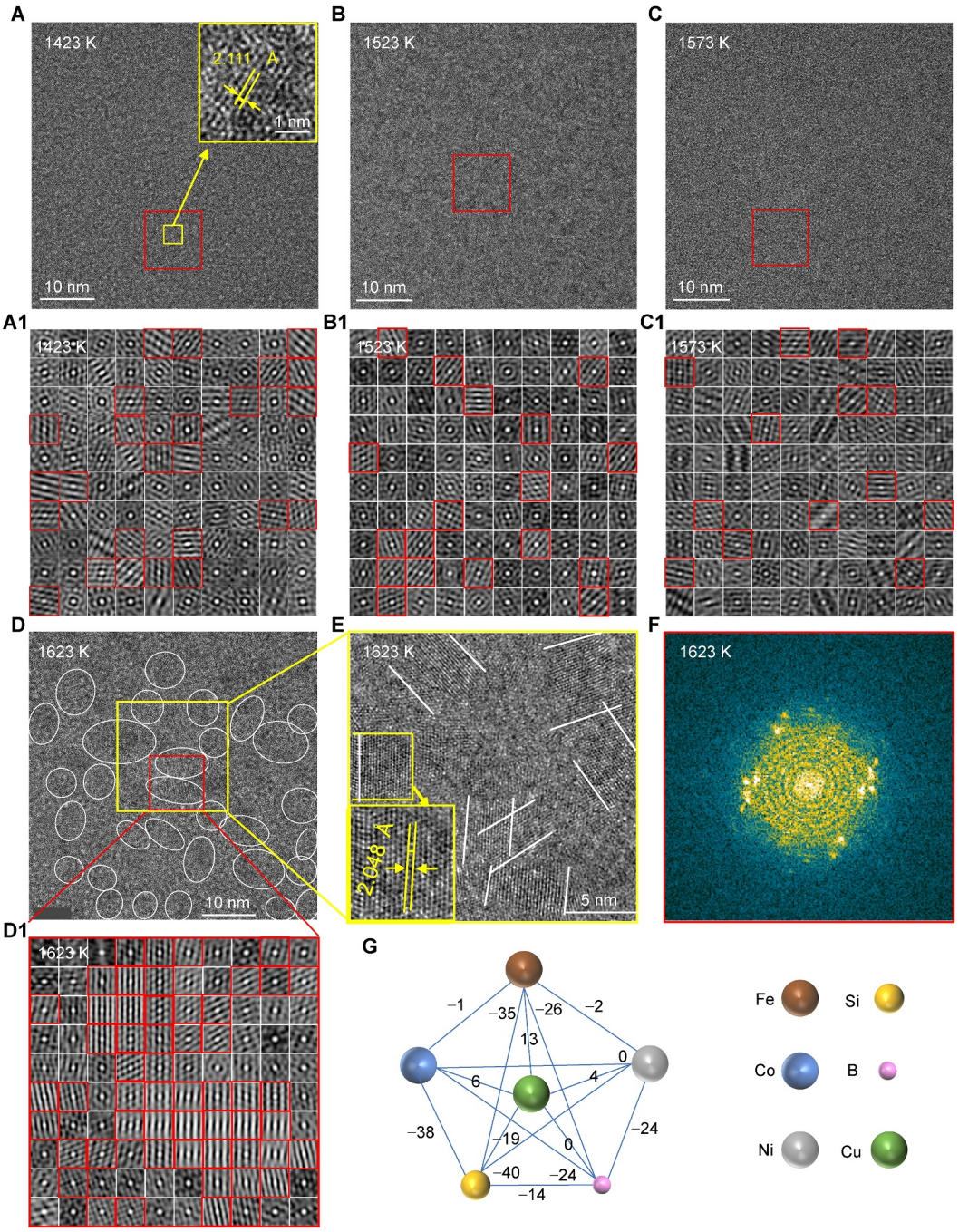

FIGURE 5 | (A–D) HRTEM images of the S1423, S1523, S1573, and S1623 samples; (A1–D1) 2D-ACF analysis of the red region in (A–D); (E) local magnification of the yellow region in (D); (F) FFT-transformed image corresponding to the red region in (D); (G) mixing enthalpy between elements.

Figure 5D shows the formation of large ordered structures (> 5 nm) in the HRTEM image of the S1623 sample, corresponding to the particle distribution observed in low-magnification TEM images. These ordered structures have been identified as Cu clusters before. Figure 5E further enlarges the yellow region in Figure 5D, confirming that the ordered structure corresponds to the (111) crystal face of Cu, thus demonstrating that high temperatures promote Cu cluster formation. Figure 5D1 presents the 2D-ACF analysis of a randomly selected region of this sample, revealing more than 50% ordered structure, with bright, symmetrical white spots in the corresponding FFT image (Figure 5F). This supports the presence of nano Cu clusters. The precipitation of larger Cu clusters acts as a reinforcing phase, significantly increasing the σ_y of the samples [20]. However, the presence of these larger Cu clusters impedes plastic deformation, and their interface with the amorphous matrix are prone to stress concentration, destabilizing the structure and promoting crack initiation.

To investigate the mechanism underlying the optimal plasticity of the S1573 sample, nanoindentation tests were performed to assess the mechanical behavior, including Young's modulus and hardness distribution, and to explore microstructural heterogeneity of the samples. Figure 6A presents the typical load-displacement

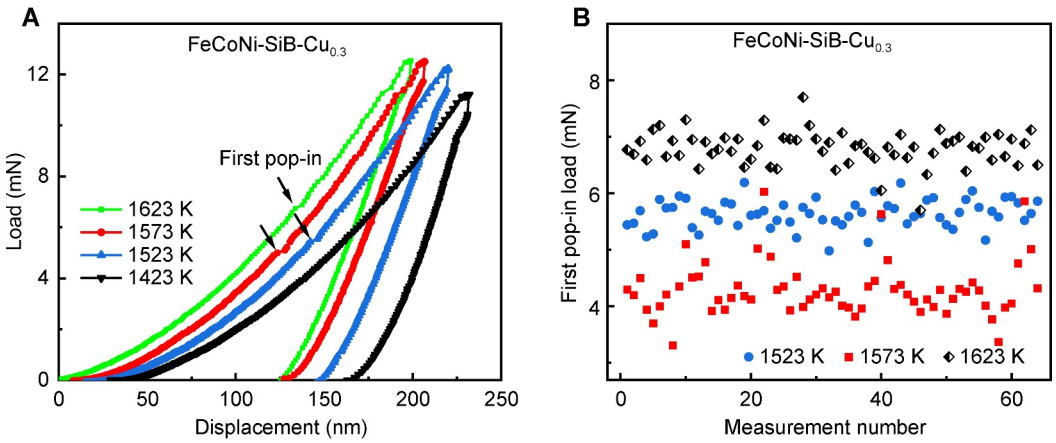

FIGURE 6 | (A) Typical load-displacement curves of the HE-BMGs samples prepared at different melt temperatures, with arrows pointing to the first pop-in event; (B) scatter plot of the first pop-in event based on 64 independent nanoindentation tests.

curves of all samples, with arrows representing the location of the first rebound event, which represents the transition from elastic to elastic–plastic behavior [21]. Among the four samples, the S1573 sample exhibited the lowest load at the first pop-in event, suggesting that it is more prone to deformation at lower stresses and thus contains more easily deformable soft zones compared to other samples. The S1523 exhibited a slightly higher load for the first pop-in event than the S1573, followed by the S1623 sample. These samples do not show any obvious structural mutation points, indicating a more homogeneous and rigid structure at the nanoscale. Based on 64 independent nanoindentation experiments, Figure 6B presents the scatter plots of the load distribution at the first pop-in event for the S1523, S1573, and S1623 samples, suggesting that the S1573 sample indeed contains more soft zones. These soft zones, due to the loose atomic arrangement, facilitate shear band nucleation, promoting the formation of multiple shear bands and favors plastic deformation [22].

Based on the above analyses, it is essential to explore the distribution of soft zones in the S1573 sample. Figure 7A, B presents the regional distribution of micro-zone Young's modulus and hardness corresponding to four samples prepared at different melt temperatures, respectively, with blue representing lower values and red representing higher values. As shown in Figure 7A, the S1423 exhibits an overall high Young's modulus, in stark contrast to the low modulus of the S1573 sample. Although low modulus typically corresponds to soft zones with large free volume [23], the broad distribution and significant fluctuation of modulus values in the S1573 sample suggest that the soft zone structure is not centrally distributed. This dispersed distribution can effectively enhance the plastic deformability of the material. In Figure 7B, many areas of low hardness and the wide range of hardness values in the S1573 sample further confirm its highly heterogeneous structural characteristics. The S1523 sample mainly exhibits overall high hardness values, although low hardness regions are also present. In addition, the S1623 sample shows numerous high-hardness areas, with its maximum hardness value significantly higher than those of the other samples, supporting its superior strength.

Nanoindentation tests can reflect the structural nonuniformity of samples but are limited in capturing structural differences at smaller scales due to the limitations of experimental manipulation. Therefore, the nanoscale viscoelastic properties (e.g., energy dissipation, elastic modulus, and adhesion) in the local region of HE-BMGs are analyzed in conjunction with the AFM testing, which offers a high spatial resolution approaching the atomic level, and provides detailed morphology information such as surface morphology [24]. The combined use of nanoindentation and AFM provides a more comprehensive understanding of structural properties of the samples. Figure 8A–D presents the 3D topography of the surface height difference for all samples. The surface height difference of the S1423, S1523 and S1573 samples are all within 1 nm. In contrast, the S1623 exhibits a height difference of about 5 nm. Noteworthily, all samples exhibited smoother surface features, ensuring that the surface roughness does not influence the nanoscale viscoelasticity measurements.

Figure 8E–H shows the local adhesion force maps of the samples prepared at different melt temperatures, revealing significant spatial nonuniformity at the nanoscale, with high adhesion forces corresponding to soft zones and low adhesion forces corresponding to hard zones [25, 26]. These samples show a similar distribution of structural inhomogeneities at the nanoscale. As shown in Figure 8E, the viscoelastic structure of the S1423 sample is primarily composed of hard zones, with soft zones embedded in them. As the melt temperature increases, the proportion of soft zones grows, eventually leading to a shift in the dominance between soft and hard zones, as shown in Figure 8F,G. The S1523 and S1573 samples exhibit significantly higher adhesion values compared to the samples prepared at low and high melt temperatures, indicating the presence of more soft deformation regions. Additionally, for the S1623 sample, the adhesion value decreases again, indicating an increase in structural brittleness.

To further investigate the effect of the melt temperature on the evolutionary of nonuniform structures at the nanoscale, the adhesion data for the samples prepared at different melt samples were quantified, and their probability density functions (PDFs) were plotted, as shown in Figure 8I–L. The results indicate that increasing the melt temperature shifts the adhesion distribution toward higher values, suggesting that higher

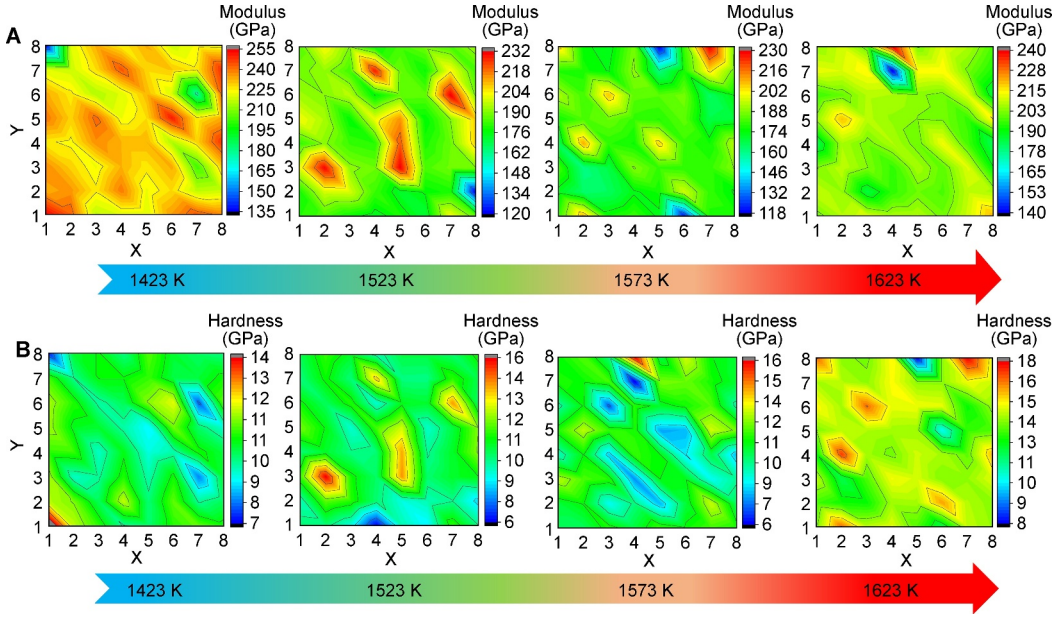

FIGURE 7 | (A) Regional distribution of nanoindentation Young's modulus; (B) regional distribution of nanoindentation hardness values for samples with different melt temperatures.

melt temperature promote a looser structure, thereby increasing the soft region. However, as shown in Figure 8L, the adhesion decreases again when the melt temperature reaches 1623 K, and this anomalous hardening behavior can be attributed to the Cu clusters observed in the TEM image. The PDF distributions of all the samples can be well fitted by two Gaussian functions, suggesting the existence of two viscoelastic modes, that is, liquid-like mode (high adhesion) and solid-like mode (low adhesion) [25, 26]. As the melt temperature increases, the viscoelastic structure shifts from a solid-like mode predominance in 1423 K to a solid-liquid-like coexistence mode at 1523 K, and finally to a liquid-like mode predominance at 1573 K. This progression explains the increase in plastic properties with the melt temperature. Similarly, the reduced plasticity and increased strength of the S1623 sample can be reasonably attributed to these structural changes.

Figure 9A illustrates the evolution of the normalized loss modulus $E''/E''_{\max}$ over the normalized temperature T/T_α at a test frequency of 1 Hz and a heating rate of 5°C $\min^{-1}$. For low melt temperatures, in addition to the primary α relaxation, two additional peaks, that is, β relaxation and β′ relaxation, are observed. The fast β′ relaxation, attributed to the vibrational motion of loosely bonded atoms constrained by more tightly bonded atoms, contrasts with the slower β relaxation, which typically represents constant loss in the low-temperature region or high-frequency domain due to its lower activation energy and weaker temperature dependence [27]. It is worth noting that Wang et al. [28] discovered that the activation energy for β′ relaxation is about half that of slow β relaxation. As a result, β′ relaxation is associated with the most mobile atoms, which induce localized inelastic events, whereas slow β relaxation involves a local but collective rearrangement of atoms, leading to localized plastic flow events, followed by the main α relaxation induced by percolation through the elastic glass matrix [27]. From Figure 9A, it is evident that the β relaxation peak for the S1573 sample exhibits the highest intensity, with its β′ relaxation peak also significantly stronger than those of the S1423, S1523, and S162 samples. This suggests that the local migration ability of atoms is the strongest in the S1573 sample, corresponding to a nonuniform structure and a higher content of free volume. The β′ relaxation peak for the S1423 sample differs from the others, likely due to the presence of crystal-like structures. The loss factor, which indicates the degree of energy dissipation during deformation, is shown in Figure 9B. The S1573 sample exhibits the highest loss factor, attributed to increased energy loss from the rapid diffusion of localized atoms during β′ relaxation. A significant peak in the loss factor is observed in all samples near the glass transition temperature, marking the transition from the amorphous state to the highly elastic state, which is a common phenomenon in MGs [27].

Based on the above analysis, we propose a mechanism explaining how melt temperature influences the plasticity of the prepared HE-BMGs. As shown in Figure 10, positive mixing enthalpies between Cu and Fe, Co and Ni promote the formation of Cu-rich or Fe/Co/Ni-rich clusters in the alloy melt. At lower melt temperatures, insufficient superheating inhibits the dispersion of MRO clusters, leading to their retention in the amorphous matrix. This contributes to stress concentrations that reduce the plasticity of the S1432 sample. Furthermore, the lack of porosity in the melt at low melt temperatures results in poor structural uniformity and a limited number of soft zones, further hindering plastic deformation of the S1432 sample. As the melt temperature increases, MRO clusters fragment into smaller SRO clusters, enabling a more homogeneous distribution of soft and hard zones in S1523 and S1573 samples. This balanced microstructure enhances plasticity through the cooperative deformation of soft and hard regions. Compared to the S1523 melt, the S1573 melt contains smaller, more dispersed clusters with looser atomic arrangements. These features are inherited by the solidified alloy, resulting in a higher density of soft zones in the S1573 sample. This facilitates the activation of multiple shear bands and improves macroscopic plasticity. However, the dominance of soft zones and the relative scarcity

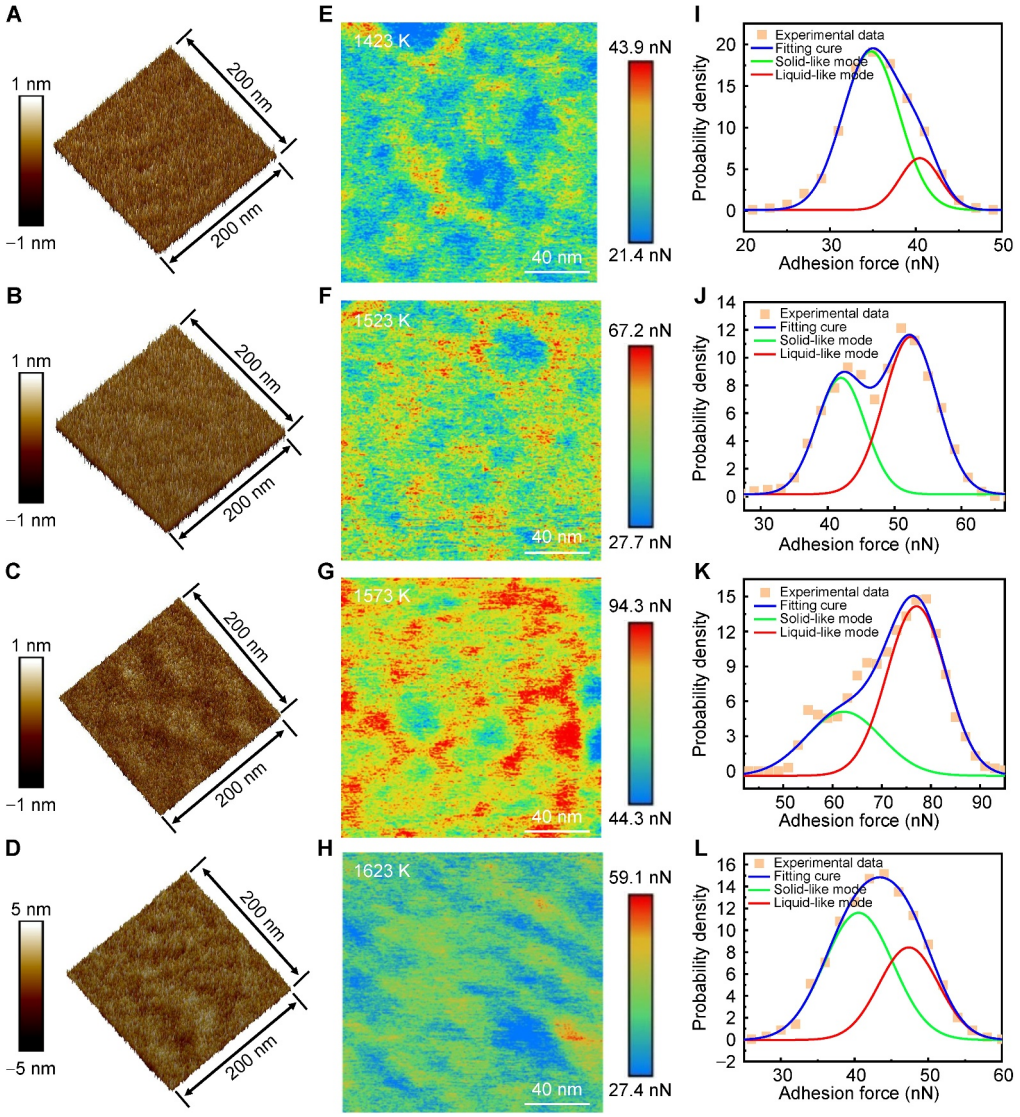

FIGURE 8 | (A–D) 3D morphology of the surface of the S1423, S1523, S1573, and S1623 samples; (E–H) 2D spatial distribution of the local adhesion force for the samples prepared at different melt temperatures; (I–L) probability density distributions of local adhesion force for samples prepared at different melt temperatures: (I) 1423 K, (J) 1523 K, (K) 1573 K, and (L) 1623 K, in which the green and red curves represent the Gaussian distribution functions corresponding to the fits for low and high adhesion forces, respectively.

of hard zones in the S1573 sample lead to a reduction in strength compared to the S1523 sample. At the melt temperature of 1623 K, large Cu clusters (> 5 nm) precipitated in the amorphous matrix. This phenomenon can be attributed to a decrease in cooling rate caused by excessively high melt temperature, which facilitates the formation of short- or medium-range ordered clusters and prolongs the time for phase separation [29]. Additionally, Sarac has shown that lower cooling rates in Cu-based bulk specimens promote the formation of Cu-rich regions during solidification [30]. Li et al. also observed that elevated temperatures significantly enhance atomic migration, causing atoms to shift from their initial positions and leading to the formation of larger nanoclusters [31]. Thus, the precipitation of Cu clusters in the high-temperature sample is considered a "self-annealing" effect, resulting from inadequate heat dissipation due to overheating, which promotes the growth of existing Cu clusters [32]. Although these large Cu clusters can enhance yield strength, they also increase the likelihood of local stress concentrations at the interfaces with the amorphous matrix, accelerating the deterioration of plasticity.

In fact, our research group has previously examined the influence of melt temperature on Zr-based MGs and found that low melt temperatures tend to promote the formation of refractory phases with long-range ordered clusters, whereas higher temperatures yield more disordered structures. Interestingly, the plasticity in those systems also peaked at intermediate temperatures—consistent with the present observations in HE-BMGs. In addition, Li et al. demonstrated that melt temperature significantly impacts the structural hierarchy of MGs, influencing both medium- and short-range order [29]. These studies collectively support our conclusion that melt temperature exerts a profound

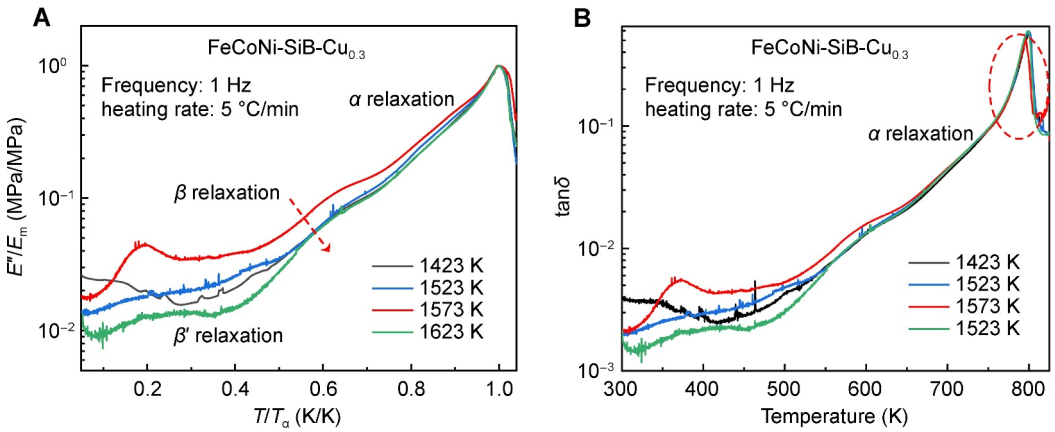

FIGURE 9 | (A) Evolution of the normalized loss modulus E''/E''_{max} as a function of normalized temperature T/T_α, and (B) variation of the loss factor (tanδ) with temperature for the samples prepared at different melt temperatures.

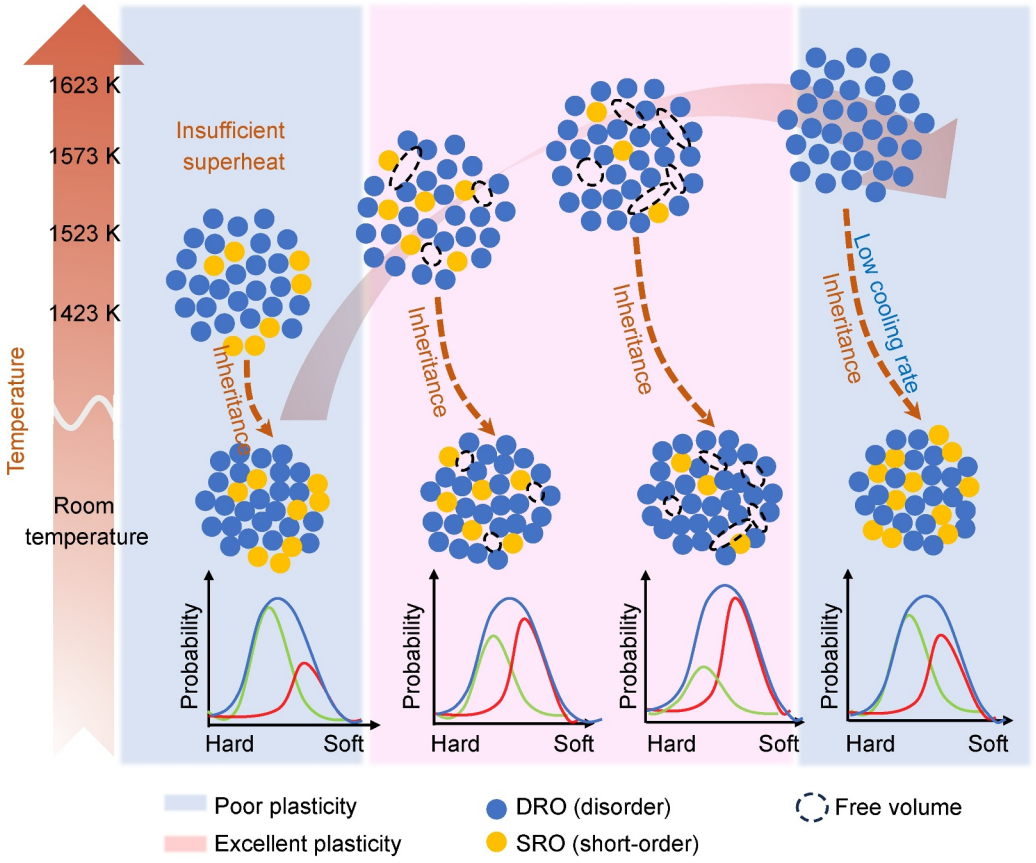

FIGURE 10 | Schematic diagram of structural evolution of the samples prepared at different melt temperatures.

effect on the structural evolution and mechanical response of amorphous alloys. Although specific responses may vary across systems due to differences in chemical composition and thermal properties, the overarching trend that optimal plasticity emerging from intermediate melt temperatures is broadly observed. Therefore, our findings contribute to a growing body of evidence, suggesting that melt temperature is a universal factor affecting the microstructure and performance of MGs, although further systematic investigations across diverse systems are necessary to refine and generalize these relationships.

4 | Conclusions

This study investigates the effect of melt temperature on the structure and mechanical properties of $[Fe_{0.25}Co_{0.25}Ni_{0.25}(Si_{0.3}B_{0.7})_{0.25}]_{99.7}Cu_{0.3}$ HE-BMGs, with the following main findings:

i. Systematic variation of melt temperatures (1423, 1523, 1573, and 1623 K) demonstrates the existence of an optimal superheating range that enhances the plasticity and thermal stability of HE-BMGs. For the present FeCoNiSiBCu

HE-BMGs, the optimal melt temperatures correspond to a superheat of 1.0–200 K.

ii. At the lower melt temperature (1423 K), the HE-BMG exhibits poor plasticity due to crystal-like cluster structures resulting from insufficient superheat, which induce stress concentrations. Nanoscale structural inhomogeneities are dominated by solid-like zones, lacking soft-zone structures necessary for plastic deformation.

iii. Melt temperatures within the optimal range promote a more uniform distribution of soft and hard zones, improving plastic deformation characteristics. Specifically, the sample prepared at 1573 K, with favorable structural nonuniformity and a larger proportion of soft zones, exhibits superior plasticity.

iv. At higher melt temperatures (1623 K), excessive superheat leads to Cu cluster precipitation (> 5 nm) in the amorphous matrix due to a "self-annealing" effect. This results in enhanced strength but compromised plasticity due to the formation of stress concentrations.

This work highlights the critical role of melt temperature in controlling the structural evolution of HE-BMGs and provides a comprehensive understanding of the relationship between melt temperature, microstructure, and mechanical properties.

Author Contributions

Xue-Ru Fan: writing – original draft, visualization. **Lei Xie:** writing – review and editing. **Qiang Li:** writing – review and editing. **Yun-He Gao:** visualization. **Chun-Tao Chang:** writing – review and editing. **Meng Gao:** writing – review and editing.

Acknowledgments

This research was supported by National Natural Science Foundation of China (Grant Nos. 52261033, 52471187, and 52201194).

Conflicts of Interest

The authors declare no conflicts of interest.

Data Availability Statement

The data that support the findings of this study are available from the corresponding author upon reasonable request.

References

1. D. C. Jiles, "Recent Advances and Future Directions in Magnetic Materials," *Acta Materialia* 51, no. 19 (2003): 5907–5939, https://doi.org/10.1016/j.actamat.2003.08.011.

2. A. Inoue, X. M. Wang, and W. Zhang, "Developments and Applications of Bulk Metallic Glasses," *Reviews on Advanced Materials Science* 18, no. 1 (2008): 1–9.

3. Q. S. Zhang, W. Zhang, G. Q. Xie, D. V. Louzguine-Luzgin, and A. Inoue, "Stable Flowing of Localized Shear Bands in Soft Bulk Metallic Glasses," *Acta Materialia* 58, no. 3 (2010): 904–909, https://doi.org/10.1016/j.actamat.2009.10.005.

4. C. Zhao, C. Dun, Q. Man, and B. Shen, "Enhancement of Plastic Deformation in FeCoNbB Bulk Metallic Glass With Superhigh Strength," *Intermetallics* 32 (2013): 408–412, https://doi.org/10.1016/j.intermet.2012.09.018.

5. S. Di, Q. Wang, J. Zhou, et al., "Enhancement of Plasticity for FeCoBSiNb Bulk Metallic Glass With Superhigh Strength Through Cryogenic Thermal Cycling," *Scripta Materialia* 187 (2020): 13–18, https://doi.org/10.1016/j.scriptamat.2020.05.059.

6. S. Singh, N. Wanderka, B. S. Murty, U. Glatzel, and J. Banhart, "Decomposition in Multi-Component AlCoCrCuFeNi High-Entropy Alloy," *Acta Materialia* 59, no. 1 (2011): 182–190, https://doi.org/10.1016/j.actamat.2010.09.023.

7. L. Jiang, H. Jiang, Y. Lu, T. Wang, Z. Cao, and T. Li, "Mechanical Properties Improvement of $AlCrFeNi_2Ti_{0.5}$ High Entropy Alloy Through Annealing Design and Its Relationship With Its Particle-Reinforced Microstructures," *Journal of Materials Science & Technology* 31, no. 4 (2015): 397–402, https://doi.org/10.1016/j.jmst.2014.09.011.

8. M. Li, H. Guan, S. Yang, Xu Ma, and Q. Li, "Minor Cr Alloyed Fe–Co–Ni–P–B High Entropy Bulk Metallic Glass With Excellent Mechanical Properties," *Materials Science and Engineering: A* 805 (2021): 140542, https://doi.org/10.1016/j.msea.2020.140542.

9. G. Kumar, T. Ohkubo, and K. Hono, "Effect of Melt Temperature on the Mechanical Properties of Bulk Metallic Glasses," *Journal of Materials Research* 24, no. 7 (2011): 2353–2360, https://doi.org/10.1557/j.jmr.2009.0272.

10. K. Mondal, T. Ohkubo, T. Toyama, Y. Nagai, M. Hasegawa, and K. Hono, "The Effect of Nanocrystallization and Free Volume on the Room Temperature Plasticity of Zr-Based Bulk Metallic Glasses," *Acta Materialia* 56, no. 18 (2008): 5329–5339, https://doi.org/10.1016/j.actamat.2008.07.012.

11. X. Cui, J. J. Li, J. C. Qiao, et al., "Relating Melting Temperature With Structure Heterogeneity and Plasticity of $Zr_{57}Cu_{20}Al_{10}Ni_8Ag_5$ Bulk Metallic Glass," *Journal of Non-Crystalline Solids* 543 (2020): 120100, https://doi.org/10.1016/j.jnoncrysol.2020.120100.

12. P. Zhu, X. Li, Q. Zhang, B. Liu, Y. Ma, and F. Zu, "Effects of Melt Temperatures on the Structure Relaxation and Compressive Plasticity of $La_{62}Al_{14}(Cu_{5/6}Ag_{1/6})_{14}(Ni_{1/2}Co_{1/2})_{10}$ Bulk Metallic Glass," *Journal of Non-Crystalline Solids* 471 (2017): 175–178, https://doi.org/10.1016/j.jnoncrysol.2017.05.036.

13. X. Fan, L. Xie, Q. Li, C. Chang, and H. Li, "Improved Plasticity of $Fe_{25}Co_{25}Ni_{25}(Si_{0.3}B_{0.7})_{25}$ High Entropy Bulk Metallic Glass Through the Addition of Cu," *Acta Metallurgica Sinica* 36, no. 3 (2022): 417–425, https://doi.org/10.1007/s40195-022-01457-9.

14. F. Xu, Y. Z. Liu, X. Sun, et al., "Percolation-Like Transition From Nanoscale Structural Heterogeneities to Shear Bands in Metallic Glass Detected by Static Force Microscopy," *Applied Surface Science* 611 (2023): 155730, https://doi.org/10.1016/j.apsusc.2022.155730.

15. Y. Shao, K. Yao, M. Li, and X. Liu, "Two-Zone Heterogeneous Structure Within Shear Bands of a Bulk Metallic Glass," *Applied Physics Letters* 103, no. 17 (2013): 171901, https://doi.org/10.1063/1.4826117.

16. S. Di, Q. Wang, Y. Yang, et al., "Efficient Rejuvenation of Heterogeneous $\{[(Fe_{0.5}Co_{0.5})_{0.75}B_{0.2}Si_{0.05}]_{96}Nb_4\}_{99.9}Cu_{0.1}$ Bulk Metallic Glass Upon Cryogenic Cycling Treatment," *Journal of Materials Science & Technology* 97 (2022): 20–28, https://doi.org/10.1016/j.jmst.2021.04.034.

17. J. Zhou, Q. Wang, Q. Zeng, et al., "A Plastic FeNi-Based Bulk Metallic Glass and Its Deformation Behavior," *Journal of Materials Science & Technology* 76 (2021): 20–32, https://doi.org/10.1016/j.jmst.2020.11.016.

18. Z. B. An, S. C. Mao, Z. Zhang, and X. D. Han, "Strengthening-Toughening Mechanism and Mechanical Properties of Span-Scale Heterostructure High-Entropy Alloy," *Acta Metallurgica Sinica* 58, no. 11 (2022): 1441–1458.

19. Q. Wang, C. T. Liu, Y. Yang, J. B. Liu, Y. D. Dong, and J. Lu, "The Atomic-Scale Mechanism for the Enhanced Glass-Forming-Ability of a

Cu-Zr Based Bulk Metallic Glass With Minor Element Additions," *Scientific Reports* 4, no. 1 (2014): 4648, https://doi.org/10.1038/j.srep.2014.04.648.

20. M. Erden, A. Erer, Ç. Odabaşi, and S. Gündüz, "The Investigation of the Effect of Cu Addition on the Nb-V Microalloyed Steel Produced by Powder Metallurgy," *Science of Sintering* 54, no. 2 (2022): 153–167, https://doi.org/10.2298/sos2202153e.

21. K. L. Johnson, *Contact Mechanics* (American Society of Mechanical Engineers, 1985).

22. Q. Hou, T. Wang, J. Zhou, X. Zhou, Qi Hao, and J. Qiao, "The Improvement of the Plasticity of a Zr – Ni – Al Bulk Metallic Glass by Static Quenching," *Materials Science and Engineering: A* 851 (2022): 143624, https://doi.org/10.1016/j.msea.2022.143624.

23. J. Zhou, S. Y. Di, B. A. Sun, et al., "Pronounced β-Relaxation in Plastic FeNi-Based Bulk Metallic Glasses and Its Structural Origin," *Intermetallics* 136 (2021): 107234, https://doi.org/10.1016/j.intermet.2021.107234.

24. C. B. Jin, Y. Z. Wu, J. N. Wang, et al., "Nanoscale Viscoelastic Transition From Solid-Like to Liquid-Like Enables Ductile Deformation in Fe-Based Metallic Glass," *Journal of Materials Science & Technology* 194 (2024): 63–74, https://doi.org/10.1016/j.jmst.2024.01.026.

25. M. Gao and J. H. Perepezko, "Mapping the Viscoelastic Heterogeneity at the Nanoscale in Metallic Glasses by Static Force Spectroscopy," *Nano Letters* 20, no. 10 (2020): 7558–7565, https://doi.org/10.1021/acs.nanolett.0c03026.

26. L. S. Huo, J. F. Zeng, W. H. Wang, C. T. Liu, and Y. Yang, "The Dependence of Shear Modulus on Dynamic Relaxation and Evolution of Local Structural Heterogeneity in a Metallic Glass," *Acta Materialia* 61, no. 12 (2013): 4329–4338, https://doi.org/10.1016/j.actamat.2013.04.004.

27. J. C. Qiao, Q. Wang, J. M. Pelletier, et al., "Structural Heterogeneities and Mechanical Behavior of Amorphous Alloys," *Progress in Materials Science* 104 (2019): 250–329, https://doi.org/10.1016/j.pmatsci.2019.04.005.

28. Q. Wang, S. T. Zhang, Y. Yang, Y. D. Dong, C. T. Liu, and J. Lu, "Unusual Fast Secondary Relaxation in Metallic Glass," *Nature Communications* 6, no. 1 (2015): 7876, https://doi.org/10.1038/ncomms8876.

29. L. Li, L. N. Hu, L. Y. Zhang, et al., "Ultra-Stable Metallic Glass Generated by Modulation of Melt State," *Rare Metals* 44, no. 3 (2025): 1917–1931, https://doi.org/10.1007/s12598-024-03026-8.

30. B. Sarac, J. T. Kim, Y. P. Ivanov, et al., "Cryo-Casting for Controlled Decomposition of Cu–Zr–Al Bulk Metallic Glass Into Nanomaterials: Implications for Design Optimization," *ACS Applied Nano Materials* 4, no. 8 (2021): 7771–7780, https://doi.org/10.1021/acsanm.1c01055.

31. H. Z. Li, S. Sohrabi, X. Li, et al., "Enhanced Magnetic Properties in a Fe-Based Amorphous Alloy Via Ultrasonic Vibration Rapid Processing," *Rare Metals* 44, no. 4 (2025): 2853–2860, https://doi.org/10.1007/s12598-024-03101-0.

32. H. Gao, Z. Li, S. Zhou, G. Zhang, and N. Cui, "The Improvement of Surface Quality and Thickness Stability of $Fe_{78}Si_9B_{13}$ Melt-Spun Ribbons by Melt Overheating," *Progress in Natural Science: Materials International* 29, no. 5 (2019): 556–560, https://doi.org/10.1016/j.pnsc.2019.08.012.